Received: 17 January 2023 | Revised: 10 November 2023 | Accepted: 21 January 2024

IET Energy Systems Integration

DOI: 10.1049/esi2.12137

ORIGINAL RESEARCH

Supercapacitor-based coordinated synthetic inertia scheme for voltage source converter-based HVDC integrated offshore wind farm

Jiebei Zhu[1] | Meiqi Shi[2] | Lujie Yu[1] | Junbo Zhao[3] | Siqi Bu[4] | Chi Yung Chung[4] | Campbell D. Booth[5]

[1]School of Electrical and Information Engineering, Tianjin University, Tianjin, China

[2]State Grid Tianjin Chengdong Electric Power Supply Company, Tianjin, China

[3]Department of Electrical and Computer Engineering, University of Connecticut, Storrs, USA

[4]Department of Electrical and Electronic Engineering, Hong Kong Polytechnic University, Kowloon, Hong Kong

[5]Department of Electronic and Electrical Engineering, University of Strathclyde, Glasgow, UK

Correspondence

Lujie Yu.
Email: lujie.yu@outlook.com

Funding information

National Natural Science Foundation of China, Grant/Award Number: 52207132; Guangdong Basic and Applied Basic Research Foundation, Grant/Award Number: 2022A1515240055

Abstract

A supercapacitor-based coordinated synthetic inertia (SCSI) scheme for a voltage source converter-based HVDC (VSC-HVDC)-integrated offshore wind farm (OWF) is proposed. The proposed SCSI allows the OWF to provide a designated inertial response to an onshore grid. Under the SCSI scheme, a supercapacitor is added to the DC side of each wind turbine generator via a bidirectional DC/DC converter, varying its voltage along with the offshore frequency to synthesise the desired inertial response. The HVDC grid side VSC employs a DC voltage/frequency droop control to convey the onshore frequency information to DC voltage without communication. Meanwhile, the wind farm side VSC regulates the offshore frequency to couple with the conveyed onshore frequency, considering voltage drop across the DC cables. An offshore frequency switching algorithm is incorporated to avoid undesired SCSI maloperation under offshore faults. The key parameters of the proposed SCSI are optimised through a small signal stability analysis. The effectiveness of the SCSI scheme is evaluated using a modified IEEE 39-bus test system. The results show that the proposed SCSI scheme can provide required inertial support from WTG-installed supercapacitors to the onshore grid through the VSC-HVDC link, significantly improving the onshore frequency stability.

KEYWORDS

frequency control, wind power plants

1 | INTRODUCTION

Nowadays, offshore wind power is rapidly developing to become one of the dominant renewable energy sources (RES) [1, 2]. Since large-scale offshore wind farms (OWFs) are distant from onshore grids, high-voltage alternating current transmission becomes technologically unapplicable due to its high capacitive charge, whereas voltage source converter-based HVDC (VSC-HVDC) transmission technology for OWFs is favoured by virtue of its offshore grid-forming capability and high control flexibility etc. [3, 4].

However, with the increasing displacement of traditional synchronous generators (SGs) by RES including OWFs, onshore grids are facing significant challenges for frequency regulation [5]. Such an issue is caused by inertia-less characteristics of various wind turbine generators (WTGs) as well as their traditional passive grid-responding control (TC) schemes [6]. A representative event was the power blackout on 9th August 2019 in Great Britain (GB), where the lack of inertia in the GB power grid under high-RES penetration resulted in a high rate of change of frequency (RoCoF) following a major grid fault, triggering anti-islanding protection relays deployed in the massive distributed generation (DG) to yield a large number of DG disconnections [7]. The DG disconnections further aggravated system power deficit with the affected grid frequency, triggering the low frequency demand disconnection

scheme. Therefore, maintaining a minimum level of system inertia is essential to ensure grid frequency stability from which OWFs shall not be excluded.

To enable RES inertial response, new grid codes and market mechanism are implemented. For instance, Hydro-Québec requires WTGs with total installed capacity greater than 10 MW to provide inertial support with minimum inertia constant of 3.5 s [8]. Stability services including inertia placement and trading are being proposed in the GB ancillary service market [9]. To enable the WTGs with the inertial response, several control strategies are proposed, which can be classified into two approaches: power reserve control [10–13] and rotor kinetic energy control [14–16]. The first approach retains a certain power reserve for inertia synthetisation by de-loading a WTG via rotor speed control [10, 11] or pitch angle control [12, 13], but this approach leads to uneconomic continuous wind power losses [17]. The second approach utilises real kinetic energy existing in WTG rotating masses by alternating WTG rotor speed; however, as WTG kinetic inertia is typically smaller than that of an SG [18], a WTG may suffer from rotor speed oscillation or even stall under extreme contingencies, threating the health of WTG mechanical components [14]. In Ref. [19], a virtual synchronous generator scheme is proposed to realise WTG inertial response by mimicking SG dynamic characteristics. But its essence is still to release the WTG kinetic energy, causing detrimental dynamic effects.

Additional energy storage can be employed to emulate inertial response for WTGs [18, 20, 21]. Batteries are employed in a wind farm to realise the inertial response following instantaneous grid RoCoF in Ref. [20], but their power discharging speed might be incompetent for emulating the fast-acting inertial response. The authors in Ref. [21] propose a coordinated scheme that parallels a superconductor magnetic energy storage (SMES) with the OWF point of common coupling to provide frequency support, but this scheme may not be economically justified given the high costs of SMES and also requires an extra converter for the SMES grid interface apart from WTG's own converter. In Ref. [18], a supercapacitor is coupled to the DC bus of a DFIG, and a synthetic inertia control strategy is proposed, but the supercapacitor energy utilisation is restricted by the narrow DC bus voltage variation range. A bidirectional DC/DC converter is employed in Refs. [22, 23] as an interface between a supercapacitor and a WTG DC bus to enhance the supercapacitor voltage variation range. However, the purpose of the scheme is to stabilise the WTG output rather than emulate an inertial response.

For an OWF integrated via a VSC-HVDC link (OWF + VSC-HVDC), it is challenging to deliver the aforementioned WTG inertial response to an onshore grid due to the frequency decoupling effect of the VSC-HVDC link [24]. To break such a decoupling barrier, several coordinated control schemes for OWF + VSC-HVDC are proposed [25–29], which can be mainly grouped as communication-based schemes and communication-free schemes. Communication-based schemes as designed in Refs. [25, 26] transmit the information of onshore grid frequency to an OWF via communication channels, but they are subject to the reliability and efficiency of the communication systems, potentially compromising the control performances. For communication-free control schemes as proposed in Refs. [27–29], the HVDC grid-side VSC (GS-VSC) linearly correlates the deviation of onshore grid frequency with the DC-link voltage regulated through elaborated droop controls. Then, the HVDC wind-farm-side VSC (WF-VSC) senses the onshore grid frequency via the instantaneous DC voltages and dynamically couples the offshore grid frequency with the onshore frequency. However, the droop control-based frequency information sensation does not consider the voltage losses arisen by DC transmission line impendences, leading to the inaccuracy of OWF inertia delivery to the onshore grid. Once again, these schemes employ the WTG rotor kinetic energy or the DC-bus-directly-coupled capacitor energy, which are not favourable options for the inertial response.

In view of these issues, this paper proposes a supercapacitor-based coordinated synthetic inertia (SCSI) scheme to enable the OWF inertial response to an onshore grid via a VSC-HVDC link, using DC/DC converter-interfaced supercapacitors in WTGs. The main features of the proposed SCSI include

1) The synthetic inertia can be 'autonomously' provided by mathematically linking the supercapacitor voltage with the offshore grid frequency under the derived SCSI control algorithm.
2) A DC voltage/frequency (u_{dc}/f) droop control loop is embedded in the GS-VSC to measure and convey instantaneous onshore grid frequency to the WF-VSC without communication. The onshore grid frequency is extracted from instantaneous DC voltage by the WF-VSC to regulate the offshore grid frequency accordingly.
3) A mode switching algorithm (MSA) is proposed for the WF-VSC to avoid inertia emulation maloperation which is subject to offshore grid faults.

The rest of the paper is organised as follows. Section 2 briefly introduces the structure and traditional control strategy of the OWF + VSC-HVDC system. The proposed SCSI scheme is detailed in Section 3. Section 4 conducts the control parameter optimisation for the SCSI scheme based on small signal stability analysis. The effectiveness of the SCSI scheme is evaluated in Section 5 using a modified IEEE 39-bus test system. Section 6 concludes the paper.

2 | OWF + VSC-HVDC SYSTEM AND ITS TRADITIONAL CONTROL

The topology of a candidate OWF + VSC-HVDC system is illustrated in Figure 1, where 200 × 5 MW permanent magnet synchronous generation (PMSG)-based WTGs are connected to an offshore AC collection system via step-up transformers. The collection system delivers the OWF generated power to an offshore WF-VSC station, which carries out AC-DC power conversion for a DC power transmission via DC cables. The

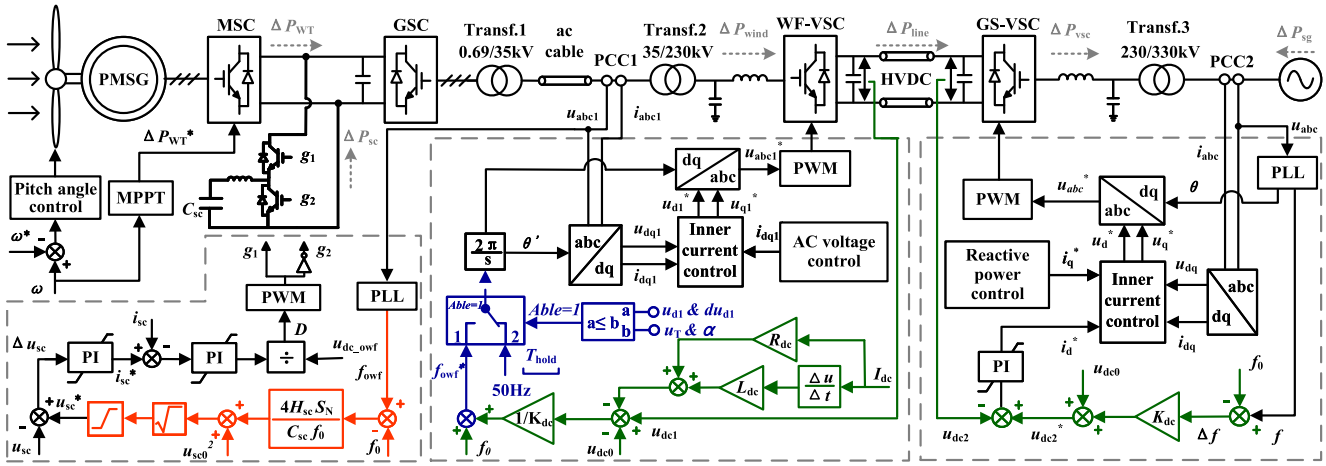

FIGURE 1 Topology and control scheme of the OWF + VSC-HVDC system.

GS-VSC receives the DC network power and converts back to AC for an onshore grid.

Under the PMSG-WTG TC scheme as shown Figure 1 [27], the machine-side converters (MSC) typically operate under an MPPT control mode, whereas the grid-side converters (GSC) regulate the DC bus voltage of the WTG energy conversion system. Under the VSC-HVDC TC scheme, the WF-VSC regulates the frequency and the amplitude of the offshore AC voltage, performing as a slack terminal for the offshore AC grid, and the GS-VSC regulates the DC network voltage to maintain a DC system power balance. Under the TC schemes, neither the OWF nor the VSC-HVDC participates in frequency support for the onshore grid.

3 | SUPERCAPACITOR-BASED COORDINATED SYNTHETIC INERTIA SCHEME FOR OWF + VSC-HVDC SYSTEM

To enable the OWF synthetic inertia to the onshore grid via the VSC-HVDC system in this section, supercapacitors are configured to the PMSG-WTGs through bidirectional DC/DC converters, and the SCSI control scheme is proposed in terms of VSC-HVDC communication-free onshore–offshore frequency coupling control, PMSG-WTG synthetic inertia control and the MSA algorithm. In addition, supercapacitor sizing and its neutral voltage setting methods are presented in this section.

3.1 | VSC-HVDC communication-free onshore-offshore frequency coupling control

As offshore frequency under the VSC-HVDC TC is decoupled from onshore frequency, the OWF is unable to detect the onshore frequency dynamics and therefore cannot provide effective inertial support to the onshore grid. To couple the offshore frequency with the onshore frequency, a communication-free frequency coupling control scheme is designed for the GS-VSC and WF-VSC, respectively, in a coordinated manner in this subsection, as highlighted in green in Figure 1:

a) In the GS-VSC control, a u_{dc}/f droop control is designed, which links the DC terminal voltage of GS-VSC with the onshore frequency.
b) In the WF-VSC control, a frequency extraction control loop is proposed to obtain the instantaneous onshore frequency based on the known DC network parameters and the DC voltage dynamics measured at the WF-VSC terminal for coupling offshore frequency with onshore frequency.

3.1.1 | GS-VSC u_{dc}/f droop control loop

To reflect real-time onshore frequency on the DC voltage, a u_{dc}/f droop control loop is implemented in the GS-VSC as follows:

$$u^*_{dc2} = K_{dc}(f - f_0) + u_{dc0} \quad (1)$$

where u_{dc2}* is the GS-VSC terminal DC voltage reference in per unit (pu), K_{dc} is a droop control coefficient, f and f_0 are the instantaneous onshore frequency and the nominal grid frequency in Hz, respectively, and u_{dc0} is the VSC-HVDC DC voltage nominal value in pu. The value of K_{dc} should be set considering the permissible deviation ranges of onshore frequency and the DC voltage, as well as the system stability margin, which will be discussed in detail in Section 4.

3.1.2 | WF-VSC frequency extraction control loop

With the u_{dc}/f control loop, the DC voltage can act as an intermediary to transfer the frequency information from the onshore grid to the offshore side. To couple the offshore

frequency with the onshore frequency, a communication-free frequency extraction control loop in the WF-VSC control is designed here, taking into account the effects of the DC network parameters.

To acquire the accurate onshore frequency information, the voltage drop across the VSC-HVDC cable, resulting from not only cable resistance but also cable inductance, is considered in this paper, different from the frequency restoration strategies as reported in [27, 28], which can be expressed as follows:

$$u_{dc1} - u_{dc2} = R_{dc} I_{dc} + L_{dc} \frac{dI_{dc}}{dt} \tag{2}$$

where u_{dc1} and u_{dc2} are the terminal DC voltages of WF-VSC and GS-VSC in pu, respectively, R_{dc} and L_{dc} are the equivalent resistance and inductance of the VSC-HVDC cable in pu, respectively, and I_{dc} is the DC current of the VSC-HVDC in pu. Due to relatively unchangeable submarine temperature, the HVDC R_{dc} and L_{dc} can be stable at manufacturing values.

Thus, the offshore frequency f_{owf}* can be regulated to couple with the onshore frequency f as per Equations (1) and (2) as follows:

$$f_{owf}{}^{*} = f_0 + \frac{u_{dc1} - u_{dc0} - R_{dc} I_{dc} - L_{dc} \frac{dI_{dc}}{dt}}{K_{dc}} \tag{3}$$

3.2 | PMSG-WTG synthetic inertia control

When the offshore frequency changes, supercapacitors in the PMSG-WTGs are required to provide synthetic inertia. This subsection designs the PMSG-WTG synthetic inertia control after associating supercapacitor power exchange dynamics with the classic SG swing equation. The specific derivation process is presented as follows.

The SG swing equation can be expressed as follows:

$$\frac{2H_{sg}}{f_0} \frac{df}{dt} = P_m - P_e = \Delta P_{sg} \tag{4}$$

where H_{sg} is the SG inertia time constant in second, P_m and P_e are the SG mechanical power input and electrical power output in pu, respectively, and ΔP_{sg} is the active power mismatch in pu.

The supercapacitor power exchange, considering its voltage u_{sc} dynamics, can be described as follows:

$$\Delta P_{sc} = \frac{C_{sc} u_{sc}}{S_n} \frac{du_{sc}}{dt} \tag{5}$$

where ΔP_{sc} is the power injected into the supercapacitor in pu, C_{sc} is the supercapacitor value in Farad, and S_n is the rated supercapacitor power capacity in VA.

To synthesise an inertia time constant H_{sc} using supercapacitors, equating (4) with (5) and integrating both sides yield

$$u_{sc}^{*} = \sqrt{\frac{4 S_n H_{sc}}{C_{sc} f_0} \left(f_{owf} - f_0 \right) + u_{sc0}^2} \tag{6}$$

where u_{sc}* is the supercapacitor voltage reference value in Volt, f_{owf} is the offshore frequency in Hz, and u_{sc0} is the neutral supercapacitor voltage in Volt.

As seen from Equation (6), to provide the synthetic inertia to the offshore grid, the supercapacitor voltage must follow the change of f_{owf} mathematically. Thus, the PMSG-WTG synthetic inertia control loop is designed based on Equation (6), as presented in the red lines in Figure 1. It is worth noting that the designed control effectively avoids the noise disturbance caused by the df/dt signal processing [5].

Under the combined actions of the former two control units in Sections 3.1 and 3.2, the inertial support mechanism of SCSI for the onshore grid is shown in Figure 2. Under normal conditions, as the onshore grid frequency deviation Δf is 0, the increments of the GS-VSC active power ΔP_{vsc}, the SG active power ΔP_{sg}, and the load power ΔP_{load} are balanced, as shown in Equation (7).

$$\Delta P_{vsc} + \Delta P_{sg} = \Delta P_{load}, \text{when } \Delta f = 0 \tag{7}$$

When the onshore frequency Δf varies, the DC voltage Δu_{dc} is controlled to change as dictated by Equation (1), reflecting the onshore frequency information to WF-VSC for offshore frequency coupling with onshore frequency by Equation (3). Thus, the supercapacitor voltage Δu_{sc} is driven by offshore frequency changes by Equation (6), correspondingly modifying the OWF active power output ΔP_{owf} for the synthetic inertial response to the onshore grid via the VSC-HVDC link.

3.3 | Mode switching algorithm of WF-VSC

When the fault occurs at the offshore grid, the power transmitted from the VSC-HVDC to the onshore grid will be interrupted. Under such cases, the primary operation of the OWF is to ride through the fault in the offshore grid securely instead of supporting the onshore grid. However, due to the

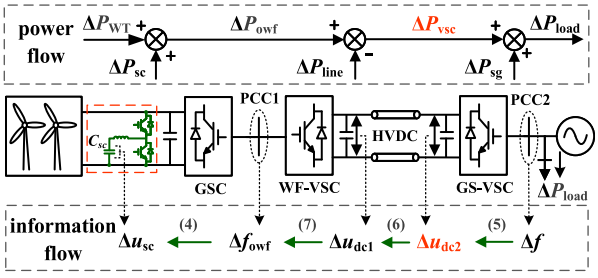

FIGURE 2 Analysis of the inertial support mechanism of supercapacitor-based coordinated synthetic inertia.

use of u_{dc}/f droop control loop, the power interruption to the onshore grid results in the DC voltage fluctuations, triggering the undesired offshore frequency change as in Equation (3) and the maloperation of the synthetic inertia.

To avoid such issue, it is necessary to maintain a constant nominal offshore frequency f_0 during an offshore fault. Thus, an MSA algorithm as shown in the blue control loop in Figure 1 is designed, which includes two operating modes: (1) Mode 1, SCSI frequency extraction control as introduced in Equation (3); and (2) Mode 2, constant frequency control. The corresponding offshore frequency reference value f_{owf}^* is determined as follows:

$$f_{owf}^* = \begin{cases} \text{Eqn. (3)}, & \text{Mode1} \\ f_0, & \text{Mode2} \end{cases} \tag{8}$$

The proposed MSA compares the amplitude u_{d1} and change rate du_{d1}/dt of the PCC1 voltage dip with preset thresholds. When u_{d1} and du_{d1}/dt are higher than their thresholds, the MSA switches from Mode 1 to Mode 2, deactivating the SCSI support to the onshore grid for a minimum duration. The activating principles of the two modes are expressed as follows:

$$\text{Mode} = \begin{cases} \text{Mode1, when } u_{d1} > u_T \ \& \ du_{d1}/dt > \alpha \\ \text{Mode2, when } u_{d1} \le u_T \ \& \ du_{d1}/dt \le \alpha \end{cases} \tag{9}$$

where u_T is the triggering threshold of the PCC1 voltage in pu, du_{d1}/dt is the PCC1 voltage change rate, and α is the threshold of the voltage change rate. The triggering thresholds can be set according to impact factors such as possible fault locations, grid topologies, and voltage dip extents. A duration T_{hold} is applied for Mode 2 to hold on for a fixed period, so as to avoid unnecessary frequent mode switching. In this paper, u_T, α and T_{hold} are set as 0.95 pu, −5 pu/s, and 200 ms, respectively.

3.4 | Supercapacitor sizing and its neutral voltage setting

To evaluate the proposed SCSI performance with various supercapacitance values, brief simulations are conducted to investigate supercapacitor voltage variations and OWF power output changes. Synthetic inertia performances with three different capacitances of $0.85C_{sc}$ (blue line in Figure 3), C_{sc} (black line) and $1.5C_{sc}$ (red line) for synthesising the same inertia time constant of $H_{sc} = 10$ s ($C_{sc} = 6.7$ F) are compared under identical grid frequency gradients. With smaller capacitance value $0.85C_{sc}$, the supercapacitor voltage is prone to reaching the DC voltage lower limit u_{scmin} as seen in Figure 3a, and the inertial response is interrupted at $t = 6.25$ s as observed in Figure 3b. However, a large capacitance value can inevitably increase the capacitor investment costs and footprints [30].

Thus, to maximise synthetic inertia effectively meanwhile minimising supercapacitor costs, the supercapacitor in this

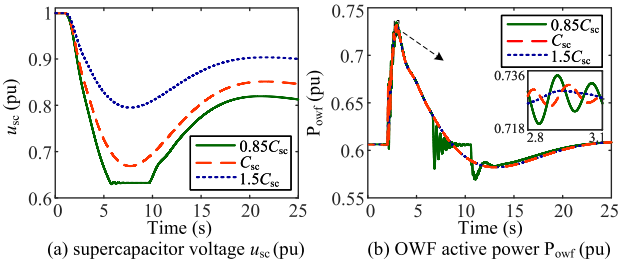

(a) supercapacitor voltage u_{sc} (pu) (b) OWF active power P_{owf} (pu)

FIGURE 3 Comparison of the system response when emulating H_{max} with different supercapacitor values: (a) supercapacitor voltage, and (b) offshore wind farm (OWF) output power.

paper is selected taking into account the maximum inertia time constant H_{max} under a covered grid frequency range $[f_{min}, f_{max}]$ as well as the permissible supercapacitor voltage variation range $[u_{scmin}, u_{scmax}]$. According to Equation (6), when the onshore frequency deviates to its limits, the supercapacitor voltage should also reach its limits as follows:

$$\begin{cases} u_{scmax} = \sqrt{\dfrac{4S_n H_{max}}{C_{sc} f_0}\left(f_{max} - f_0\right) + u_{sc0}^2} \\ u_{scmin} = \sqrt{\dfrac{4S_n H_{max}}{C_{sc} f_0}\left(f_{min} - f_0\right) + u_{sc0}^2} \end{cases} \tag{10}$$

From Equation (10), the optimal supercapacitor value C_{sc} can be obtained as follows:

$$C_{sc} = \frac{4S_n H_{max} \Delta f_{max}}{f_0\left(u_{scmax}^2 - u_{scmin}^2\right)} \tag{11}$$

where $\Delta f_{max} = f_{max} - f_{min}$ refers to the frequency deviation range in Hz.

In addition, the neutral supercapacitor voltage setpoint u_{sc0} can also be obtained from Equation (10) as follows:

$$u_{sc0} = \sqrt{\frac{f_{max} - f_0}{\Delta f_{max}} u_{scmax}^2 + \frac{f_0 - f_{min}}{\Delta f_{max}} u_{scmin}^2} \tag{12}$$

From Equation (12), it can be deferred that the neutral supercapacitor voltage setpoint should be appropriately selected considering $[f_{min}, f_{max}]$ and $[u_{scmin}, u_{scmax}]$.

Figure 4 visualises the three-dimensional relationship among C_{sc}, H_{max} and Δf_{max} under various $[u_{scmin}, u_{scmax}]$. Similarly, when synthesising an identical H_{max}, a larger C_{sc} is required for a larger Δf_{max} or a narrower $[u_{scmin}, u_{scmax}]$. It can also be observed that a wider $[u_{scmin}, u_{scmax}]$ (e.g. ± 30%) by virtue of the bidirectional DC/DC converter can effectively reduce the capacitor footprint and investment cost compared to a narrower $[u_{scmin}, u_{scmax}]$ (e.g. ± 15%) when the supercapacitor is directly attached to the DC-link of the WTG without a DC/DC converter as reported in Ref. [18]. The cost can be paid off over a long term by inertial response products intensified by ancillary markets [31].

4 | SMALL SIGNAL ANALYSIS OF SCSI SCHEME

To optimise the SCSI control parameters, this section establishes a small signal model (SSM) of the power system as illustrated in Figure 1, with the detailed parameters of OWF, VSC-HVDC and SG presented in Appendix A Tables A1–A3.

The system SSM is established based on the state-space modular subsystems of the circuits and control systems which are connected as in Figure 5, with the matrix equations presented in Appendix B. The linearised form of the SSM, obtained with the aid of the linear analysis tool in MATLAB/Simulink [32], can be expressed as follows:

$$\frac{d}{dt}\Delta\mathbf{X} = \mathbf{A}\Delta\mathbf{X} + \mathbf{B}\Delta\mathbf{U} \tag{13}$$

where Δ represents small perturbation changes, $\mathbf{A}$ is the state matrix, $\mathbf{B}$ is the input/control matrix, $\mathbf{X}$ is the state vector and $\mathbf{U}$ is the input vector.

The system SSM accuracy is verified by comparing its step responses to those from its electromagnetic transient (EMT) model simulated in MATLAB/Simulink [33]. As the active power reference of the SG turbine governor is stepped down by 0.1 pu at $t = 1$ s, as seen from Figure 6, the SSM responses are aligned with those from the EMT model, demonstrating the SSM accuracy.

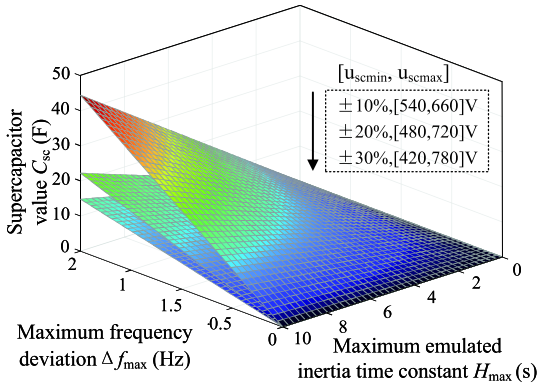

FIGURE 4 The three-dimensional relationship of C_{sc}-H_{max} -Δf_{max}.

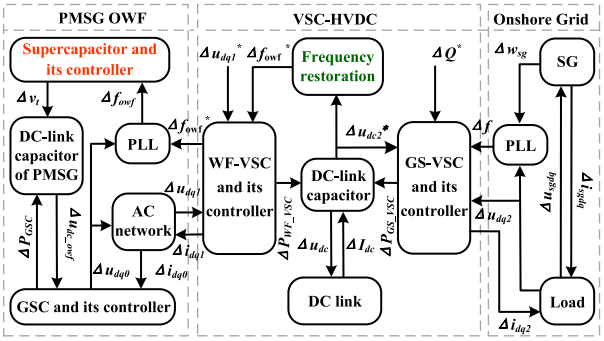

FIGURE 5 Small signal model interface diagram of the OWF + VSC-HVDC system with the supercapacitor-based coordinated synthetic inertia scheme.

With the SSM, the system eigenvalues are obtained as listed in Appendix A Table A5. The system modes λ_3 & λ_4, λ_6 & λ_7, λ_{12} & λ_{13}, and λ_{15} & λ_{16} are identified as the dominant modes to be focused. Due to the space constraint, the two important SCSI parameter optimisations of synthetic inertia time constant H_{sc} and u_{dc}/f droop gain are conducted. Other optimised control parameters are presented in Appendix A Table A4.

4.1 | Stability impact of SCSI synthetic inertia time constants

As shown in Figure 7a, with the H_{sc} increase from 0 to 40 s, the dominant λ_3 & λ_4, λ_6 & λ_7 and λ_{12} & λ_{13} all move close to the imaginary axis, indicating a reduced stability. When λ_{12} & λ_{13} intersect with the imaginary axis and the damping ratio reduces to 0 at H_{sc} = 36 s, the system is critically stable, implying that the maximum H_{sc} can be set as 36 s.

As confirmed by Figure 7b, under a 1% load increase at the onshore grid, the OWF can stably provide inertial power when H_{sc} = 6 s and H_{sc} = 10 s, respectively. However, when H_{sc} = 36 s, significant OWF inertial power oscillations are observed, which is consistent with the analysis conclusion.

4.2 | Optimisation for u_{dc}/f droop gain

Figure 8a shows that with the K_{dc} increase from 0.2 to 5, the dominant λ_{12} & λ_{13} dramatically shift, initially moving away from the imaginary axis and then towards the imaginary axis. When K_{dc} = 1.2, λ_{12} & λ_{13} are located furthest from the

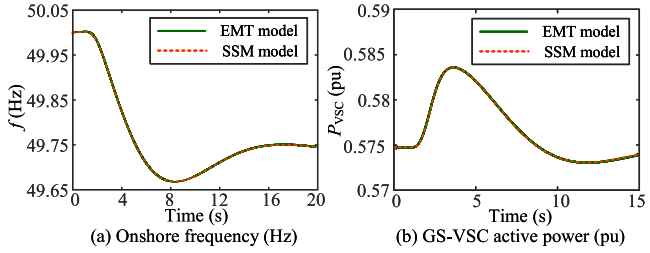

FIGURE 6 Step response comparisons between the EMT model and SSM model: (a) Onshore frequency and (b) GS-VSC active power.

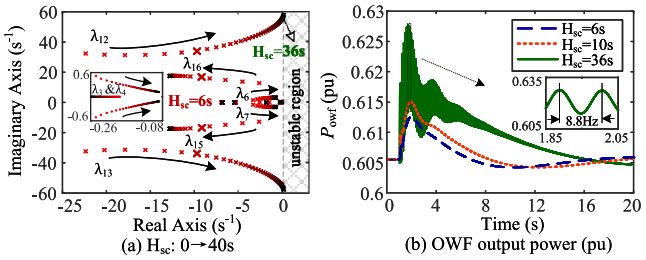

FIGURE 7 Dominant eigenvalue locis and dynamic response with H_{sc} vary: (a) H_{sc} varies from 0 to 40 s and (b) offshore wind farm output power.

imaginary axis, and the system has the strongest damping, identifying the optimal K_{dc}.

Furthermore, considering a secured grid operational frequency range typically as ± 1 Hz (±2%) [17], when $K_{dc} = 1.2$, the maximum DC voltage deviation is correspondingly calculated as ± 2.4% under the desgined u_{dc}/f droop control. Such DC voltage deviation is acceptable considering the permissible voltage variation range typically as ± 10% [5].

Figure 8b presents that after a 1% load increase, with the optimal $K_{dc} = 1.2$, the onshore grid frequency oscillation is the smallest compared to those with the smaller and larger K_{dc}.

5 | SIMULATION RESULTS

To evaluate SCSI performance, a modified IEEE 39-bus system as shown in Figure 9 is simulated in the PSCAD/EMTDC platform. The SGs at for the total systembuses 39, 38 and 32 are replaced by three identical aggregated 1000 MVA-rated OWF + VSC-HVDC systems (as shown in Figure 1) under the SCSI scheme, accounting for 35% of the total system-installed generation capacity. The circuit and control parameters of the OWF + VSC-HVDC system are presented in Appendix A Tables A1–A4. A switchable load L1 at bus 16 is modelled as the resistive load of $P_L + jQ_L = 574$ MW + j25 MVar (5% of the total load) to create a step load change event. By setting $\Delta f_{max} = 2$ Hz, $H_{max} = 10$ s, $[u_{scmin}, u_{scmax}] = [400$ V, 800V] in Equation (12), the optimal capacitance for the WTG is selected as $C_{sc} = 6.7$ F.

Four cases are compared to evaluate the performance of the proposed SCSI scheme: Case A of a load increase in the onshore grid; Case B of a wind power rise; Case C of an onshore grid fault; and Case D of an offshore grid fault.

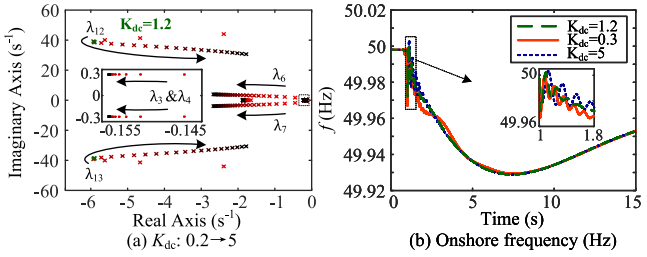

FIGURE 8 Dominant eigenvalue locis and dynamic response with K_{dc} vary: (a) K_{dc} varies from 0.2 to 5 and (b) Onshore frequency.

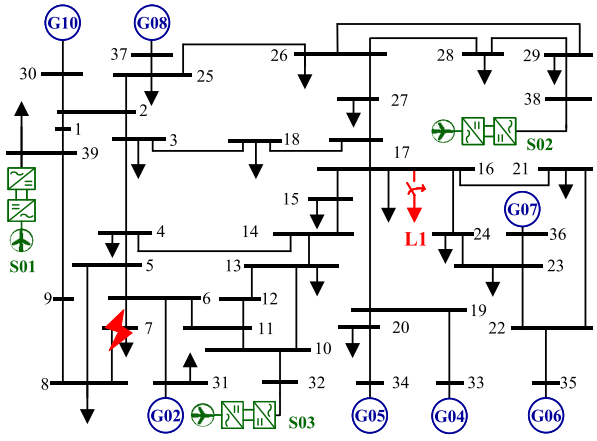

FIGURE 9 Single-line diagram of the simulated IEEE 39-bus test system.

5.1 | Onshore load increase

The load L1 is switched in at $t = 1$ s, and the system responses under SCSI and TC are illustrated in Figure 10. Under TC, the onshore frequency decreases from 50 to 49.45 Hz immediately after the load increase while the offshore frequency is maintained at a constant value of 50 Hz due to the VSC-HVDC decoupling effect, as seen from Figures 10a,c, respectively. The OWF under TC does not provide inertial support for the onshore grid as shown in Figures 10g,h.

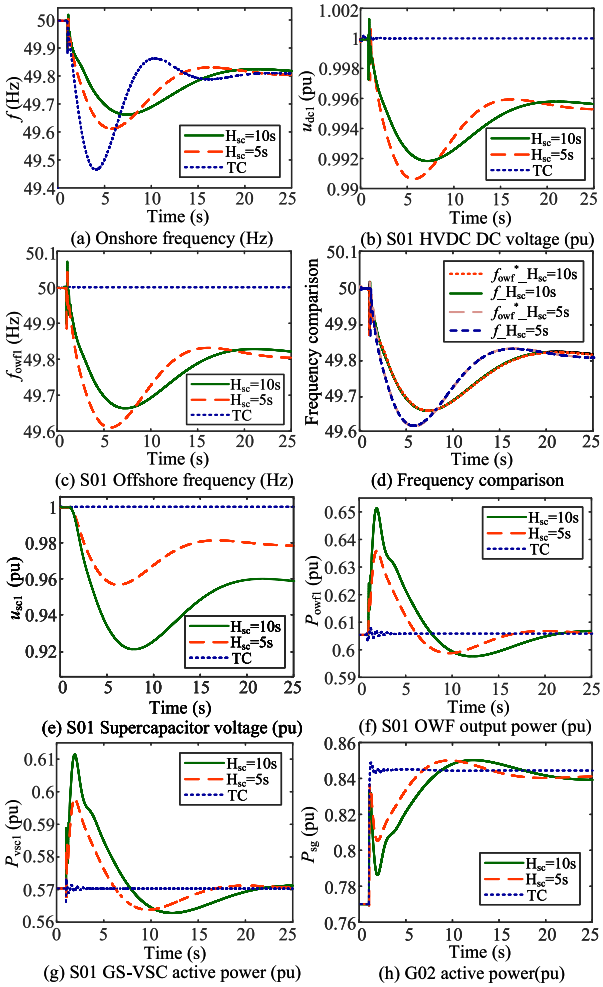

FIGURE 10 Comparison of the supercapacitor-based coordinated synthetic inertia (SCSI) and TC response for a 5% load increase: (a) Onshore frequency; (b) S01 HVDC DC voltage; (c) S01 Offshore frequency; (d) Frequency comparison; (e) S01 Supercapacitor voltage; (f) S01 offshore wind farm (OWF) active power; (g) S01 GS-VSC active power; and (h) G02 active power.

In contrast, under SCSI, the onshore frequency as seen in Figure 10a experiences a significant reduction in both magnitude deviation and RoCoF. Also, Figure 10a demonstrates that a lager synthetic inertia H_{sc} is more favourable to the onshore frequency stability. Moreover, SCSI can effectively ease the power surge of the onshore G02, as observed in Figure 10h, being beneficial to its stable operation.

Such frequency support is achieved by the combined actions of the PMSG-WTG synthetic inertia and VSC-HVDC control coordination with the details as follows: After the step load increase, the DC voltage is dictated by the u_{dc}/f droop control loop in the GS-VSC control of Equation (1), incurring a minor drop to reflect the onshore frequency dynamics as observed in Figure 10b. Then, the offshore frequency is regulated as (3) in the WF-VSC control to ensure its consistency with the extracted information of the onshore frequency, as depicted in Figures 10c,d. Then, the PMSG-WTG senses the offshore frequency variation and the supercapacitor controlled by the synthetic inertia control loop as in Equation (6) to discharge as observed in Figure 10e, providing inertial power to the onshore grid through the offshore grid and VSC-HVDC, see Figures 10f,g.

5.2 | Wind speed rise

Figure 11 compares the performances of SCSI and TC under wind speed rise from 10 m/s to 10.5 m/s at $t = 1$ s in S01, leading to the increase in the OWF and GS-VSC exported active power as seen in Figures 11f,g. Such power increase results in a power imbalance in the onshore grid. Compared to TC, SCSI significantly slows down the onshore grid RoCoF and reduces the onshore frequency deviation as shown in Figure 11a. Figure 11b illustrates that the DC voltage increases accordingly during the onshore frequency increase, acting as an intermediary to transfer the onshore frequency to offshore. As seen in Figure 11c, the offshore frequency is adjusted by the WF-VSC control of (3) to realise the onshore and offshore frequency coupling as proven in Figure 11d. Meanwhile, the supercapacitor in PMSG-WTG is charged during the offshore frequency increase (Figure 11e), reducing the OWF output power and the power injected into the onshore grid via the VSC-HVDC, see Figures 11f,g. Again, as shown in Figure 11h, SCSI alleviates the sudden decrease in the G02 active power output.

5.3 | Onshore grid fault

A 100 ms three-phase-to-ground fault is applied at busbar 7 at the onshore grid at $t = 1$ s, resulting in a 20% voltage dip as shown in Figure 12a. The proposed SCSI scheme, due to the coordinated effect of the VSC-HVDC frequency coupling control and the OWF synthetic inertia control, significantly reduces the onshore frequency deviation as well as the frequency recovery time as seen in Figure 12b compared to TC. Figure 12c presents that the DC voltage under SCSI is

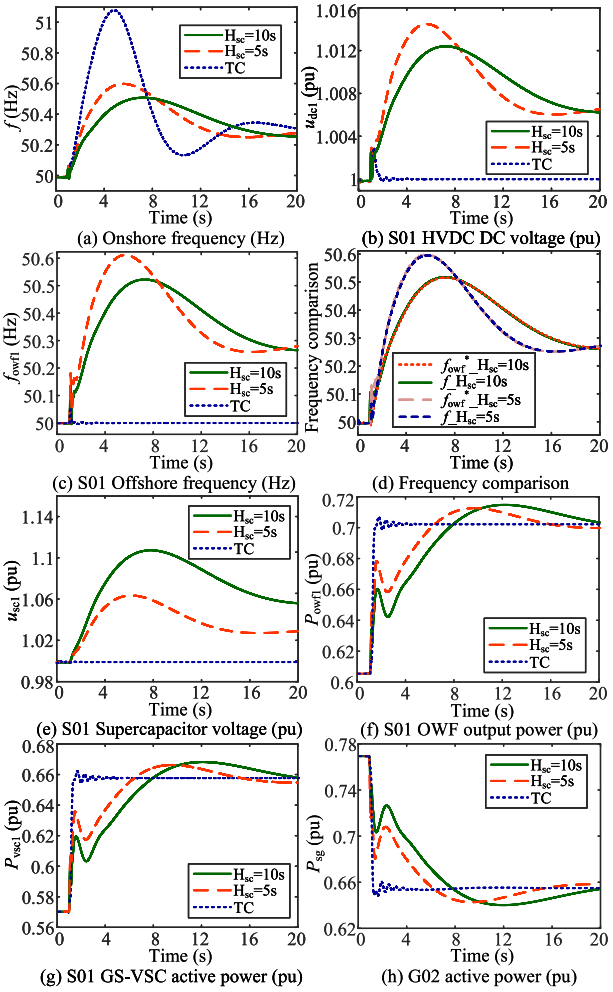

FIGURE 11 Comparison of the supercapacitor-based coordinated synthetic inertia (SCSI) and TC response for a wind speed change from 10 m/s to 10.5 m/s: (a) Onshore frequency; (b) S01 HVDC DC voltage; (c) S01 Offshore frequency; (d) Frequency comparison; (e) S01 Supercapacitor voltage; (f) S01 offshore wind farm (OWF) active power; (g) S01 GS-VSC active power; and (h) G02 active power.

controlled to vary, reflecting the onshore grid frequency dynamics to the WF-VSC DC terminal. The onshore frequency information is restored and mirrored to offshore frequency by the WF-VSC control, as shown in Figure 12e, despite a trivial transient discrepancy. Due to the synthetic inertia control, the voltage of the PMSG-WTG supercapacitors follows the offshore frequency variation to provide inertial power for the onshore grid, as seen in Figures 12f–h.

5.4 | Offshore grid fault

A temporary 100 ms three-phase-to-ground fault is applied at S01 PCC1 in the offshore grid at $t = 1$ s. Figure 13 compares the SCSI performances of $H_{sc} = 10$ s with and without the proposed MSA algorithm. It can be seen that from Figure 13a, the fault results in an approximate 18% voltage dip at PCC1, and the power transmitted from the VSC-HVDC to the onshore grid is affected (Figure 13h). Without the MSA algorithm, due to the

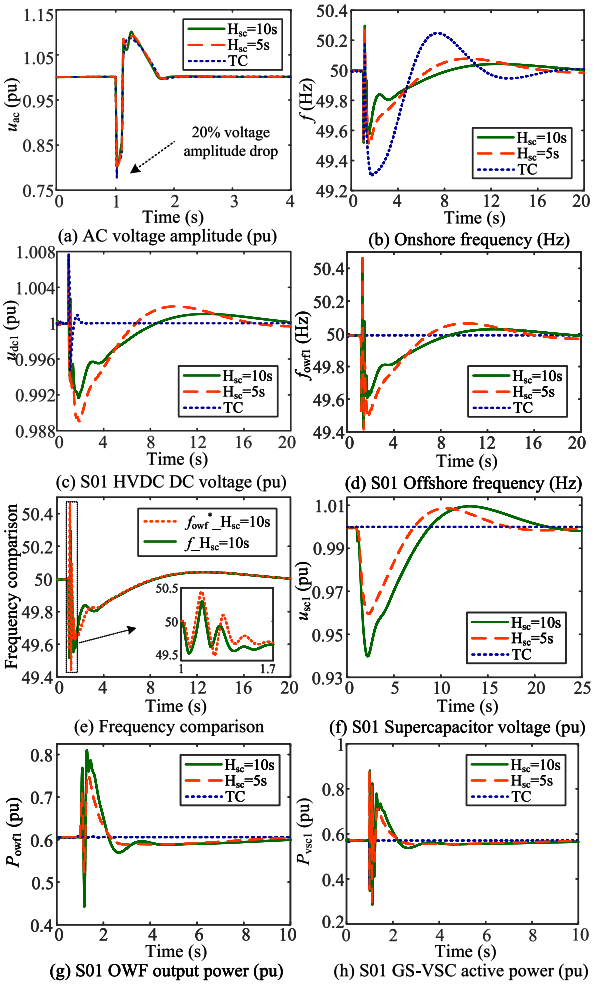

FIGURE 12 Comparison of the supercapacitor-based coordinated synthetic inertia (SCSI) and TC response for a 100 ms three phase-to-ground fault at busbar 7: (a) AC voltage amplitude; (b) Onshore frequency; (c) S01 HVDC DC voltage; (d) S01 Offshore frequency; (e) Frequency comparison; (f) S01 Supercapacitor voltage; (g) S01 offshore wind farm (OWF) active power; and (h) S01 GS-VSC active power.

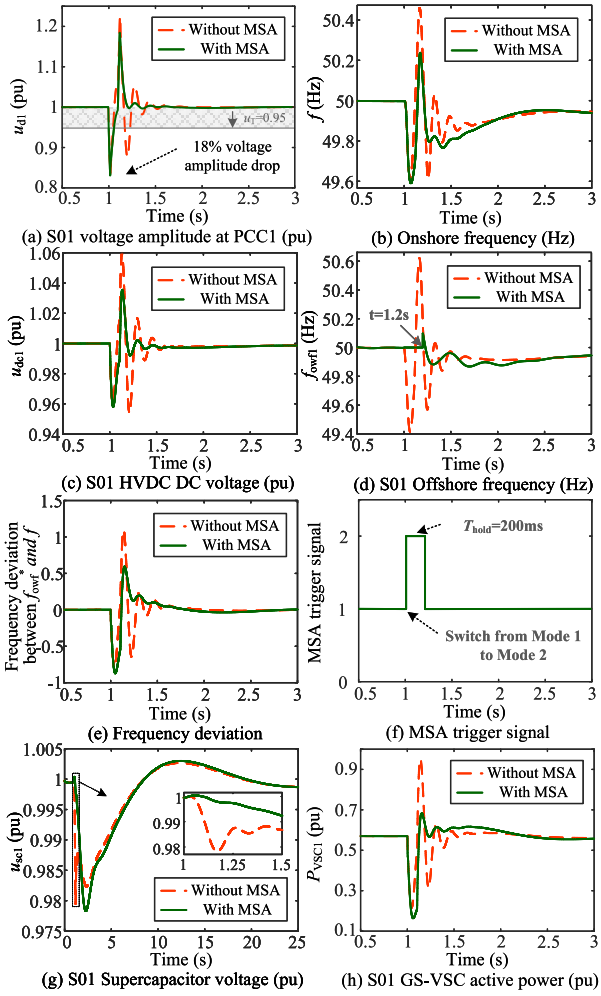

FIGURE 13 The mode switching algorithm (MSA) performance under a 100 ms three phase-to-ground fault at S01 PCC1: (a) S01 voltage amplitude at PCC1; (b) Onshore frequency; (c) S01 HVDC DC voltage; (d) S01 Offshore frequency; (e) Frequency deviation between f_{owf1} and f; (f) MSA trigger signal; (g) S01 Supercapacitor voltage; and (h) S01 GS-VSC active power.

use of the u_{dc}/f droop control loop, the VSC-HVDC delivered power to the onshore grid results in an offshore frequency change as seen in Figure 13b and in turn leads to undesirable DC voltage fluctuations as shown in Figure 13c. Such DC voltage variation cannot correctly reflect the onshore frequency information, leading to the discrepancy between the real onshore frequency and the WF-VSC extracted one as in Figure 13e. This can adversely affect the system inertial response and overall stability, which is consistent with the analysis in Section 3.3. With the MSA algorithm activated, as the amplitude and change rate of PCC1 voltage dip are higher than the triggering thresholds of 0.95 pu and −5 pu/s as set in Equation (9), respectively, the WF-VSC switches from Mode 1 to Mode 2 immediately to regulate the offshore frequency at 50 Hz, as shown in Figures 13d,f. Mode 2 lasts for 200 ms of the preset holding duration T_{hold} as designed in Section 3, avoiding unnecessary frequent mode switching actions. During the Mode 2 holding period, the frequencies of the offshore grid and the onshore grid are decoupled, so that the offshore fault less affects the onshore frequency and the DC voltage as observed in Figures 13b,c. Moreover, the supercapacitor voltage is nearly unchanged during the fault period as seen in the zoomed view of Figure 13g under the stable offshore frequency at 50 Hz, alleviating the adverse effect of the inertia emulation maloperation. Noticeably, the MSA algorithm also mitigates the oscillation of GS-VSC active power, as observed in Figure 13h.

6 | CONCLUSION

This paper proposes a SCSI scheme for the voltage source converter-based HVDC-integrated OWF system (OWF + VSC-HVDC) to provide flexible and secured inertial support for an onshore grid. The appropriately-sized supercapacitor, as the inertial energy source, is connected to the DC side of each WTG via a bidirectional DC/DC converter to maximise its accessible energy. The SCSI scheme consists of the following three core control units:

1) VSC-HVDC communication-free onshore-offshore frequency coupling control: A DC voltage/frequency droop control in grid side VSC (GS-VSC) and a frequency extraction control in wind farm side VSC (WF-VSC) are adopted to couple the offshore frequency with the onshore frequency based on the known DC network parameters without communication, enabling the OWF to detect onshore frequency contingencies.
2) PMSG-WTG synthetic inertia control: A supercapacitor voltage variation algorithm is derived to synthesise the SG (SG) inertial response after associating supercapacitor electrical dynamics with the SG swing equation, mathematically linking the supercapacitor voltage with the offshore frequency in real time. Such control avoids processing df/dt signals which can easily cause undesirable control noise.
3) WF-VSC MSA: The MSA algorithm is incorporated in WF-VSC control to avoid SCSI maloperation during the offshore grid fault by monitoring the amplitude and change rate of the offshore grid voltage dip.

It is concluded from the simulation verification that the proposed SCSI scheme can effectively and securely improve the onshore frequency stability under the conditions of load increase, wind speed rise, onshore and offshore grid fault. With rapidly reduced system kinetic energy in the future, the SCSI scheme can enhance the overall system inertia level and guarantee the frequency stability.

ACKNOWLEDGEMENTS

This work is supported by National Natural Science Foundation of China, (Grant/Award Number: 52207132) and Guangdong Basic and Applied Basic Research Foundation, (Grant/Award Number: 2022A1515240055).

CONFLICT OF INTEREST STATEMENT

None.

DATA AVAILABILITY STATEMENT

Data sharing not applicable to this article as no datasets were generated or analysed during the current study.

REFERENCES

1. Global Wind Report 2021. Global Wind Energy Council (GWEC). Tech. Rep. (2021)
2. Rodríguez-Amenedo, J.L., et al.: Control of the parallel operation of vsc-hvdc links connected to an offshore wind farm. IEEE Trans. Power Deliv. 34(1), 32–41 (2019). https://doi.org/10.1109/tpwrd.2018.2841908
3. Kou, P., et al.: Frequency support from a dc-grid offshore wind farm connected through an hvdc link: a communication-free approach. IEEE Trans. Energy Convers. 33(3), 1297–1310 (2018). https://doi.org/10.1109/tec.2018.2814604
4. Shao, B., et al.: Sub-synchronous oscillation characteristics and analysis of direct-drive wind farms with vsc-hvdc systems. IEEE Trans. Sustain. Energy 12(2), 1127–1140 (2021). https://doi.org/10.1109/tste.2020.3035203
5. Zhu, J., et al.: Inertia emulation control strategy for vsc-hvdc transmission systems. IEEE Trans. Power Syst. 28(2), 1277–1287 (2013). https://doi.org/10.1109/tpwrs.2012.2213101
6. Adeuyi, O.D., et al.: Fast frequency response from offshore multiterminal vsc–hvdc schemes. IEEE Trans. Power Deliv. 32(6), 2442–2452 (2017). https://doi.org/10.1109/tpwrd.2016.2632860
7. Technical report on the events of 9 august 2019: National Grid UK. Tech. Rep. (2019)
8. Transmission Provider Technical Requirements For The Connection Of Power Plants To The Hydro-Quebec Transmission System. Tech. Rep. Hydro Quebec TransEnergie (2009)
9. Tech. Rep. [Online]. https://www.nationalgrideso.com/future-energy/projects/stability-market-design
10. Vidyanandan, K.V., Senroy, N.: Primary frequency regulation by deloaded wind turbines using variable droop. IEEE Trans. Power Syst. 28(2), 837–846 (2013). https://doi.org/10.1109/tpwrs.2012.2208233
11. Ma, S., et al.: Clustering-based coordinated control of large-scale wind farm for power system frequency support. IEEE Trans. Sustain. Energy 9(4), 1555–1564 (2018). https://doi.org/10.1109/tste.2018.2794622
12. Wang, T., et al.: A new control strategy of dfig-based wind farms for power system frequency regulation. In: 2015 IEEE PES Asia-Pacific Power and Energy Engineering Conference (APPEEC), pp. 1–5 (2015)
13. Wu, Z., et al.: A coordinated primary frequency regulation from permanent magnet synchronous wind turbine generation. In: 2012 IEEE Power Electronics and Machines in Wind Applications, pp. 1–6 (2012)
14. Lee, J., et al.: Releasable kinetic energy-based inertial control of a dfig wind power plant. IEEE Trans. Sustain. Energy 7(1), 279–288 (2016). https://doi.org/10.1109/tste.2015.2493165
15. Hwang, M., et al.: Dynamic droop–based inertial control of a doubly-fed induction generator. IEEE Trans. Sustain. Energy 7(3), 924–933 (2016). https://doi.org/10.1109/tste.2015.2508792
16. Wu, Y.-K., et al.: Frequency regulation at a wind farm using time-varying inertia and droop controls. IEEE Trans. Ind. Appl. 55(1), 213–224 (2019). https://doi.org/10.1109/tia.2018.2868644
17. Lu, Z., Ye, Y., Qiao, Y.: An adaptive frequency regulation method with grid-friendly restoration for vsc-hvdc integrated offshore wind farms. IEEE Trans. Power Syst. 34(5), 3582–3593 (2019). https://doi.org/10.1109/tpwrs.2019.2901986
18. Zhu, J., et al.: Synthetic inertia control strategy for doubly fed induction generator wind turbine generators using lithium-ion supercapacitors. IEEE Trans. Energy Convers. 33(2), 773–783 (2018). https://doi.org/10.1109/tec.2017.2764089
19. Huang, L., et al.: Synchronization and frequency regulation of dfig-based wind turbine generators with synchronized control. IEEE Trans. Energy Convers. 32(3), 1251–1262 (2017). https://doi.org/10.1109/tec.2017.2675480
20. Liu, R., Wang, Z., Xing, H.: Virtual inertia control strategy for battery energy storage system in wind farm. 2019 IEEE PES Asia-Pacific Power and Energy Engineering Conference (APPEEC), 1–5 (2019)
21. Miao, L., et al.: Coordinated control strategy of wind turbine generator and energy storage equipment for frequency support. IEEE Trans. Ind. Appl. 51(4), 2732–2742 (2015). https://doi.org/10.1109/tia.2015.2394435
22. Qu, L., Qiao, W.: Constant power control of dfig wind turbines with supercapacitor energy storage. IEEE Trans. Ind. Appl. 47(1), 359–367 (2011). https://doi.org/10.1109/tia.2010.2090932
23. Mandic, G., et al.: Lithium-ion capacitor energy storage integrated with variable speed wind turbines for power smoothing. IEEE J. Emerg. Sel. Topics Power Electron. 1(4), 287–295 (2013). https://doi.org/10.1109/jestpe.2013.2284356
24. Kabsha, M.M., Rather, Z.H.: A new control scheme for fast frequency support from hvdc connected offshore wind farm in low-inertia system. IEEE Trans. Sustain. Energy 11(3), 1829–1837 (2020). https://doi.org/10.1109/tste.2019.2942541
25. Lu, G.L., Lin, C.-H., Wu, Y.-K.: Comparison of communication-based and coordination-based frequency control schemes for hvdc-connected offshore wind farms. IEEE Trans. Ind. Appl. 57(4), 3352–3365 (2021). https://doi.org/10.1109/tia.2021.3079233
26. Lin, C.H., Wu, Y.-K.: Overview of frequency control technologies for wind power systems. pp. 272–275, (2020)
27. Li, Y., et al.: Coordinated control of wind farm and vsc-hvdc system using capacitor energy and kinetic energy to improve inertia level of power systems. Int. J. Electr. Power Energy Syst. 59, 79–92 (2014). https://doi.org/10.1016/j.ijepes.2014.02.003
28. Liu, X., Lindemann, A.: Control of vsc-hvdc connected offshore windfarms for providing synthetic inertia. IEEE J. Emerg. Sel. Topics Power

Electron. 6(3), 1407–1417 (2018). https://doi.org/10.1109/jestpe.2017.2751541
29. Li, Y., et al.: Coordinated control strategies for offshore wind farm integration via vsc-hvdc for system frequency support. IEEE Trans. Energy Convers. 32(3), 843–856 (2017). https://doi.org/10.1109/tec.2017.2663664
30. Shen, Z., et al.: Variable-inertia emulation control scheme for vsc-hvdc transmission systems. IEEE Trans. Power Syst. 37(1), 629–639 (2022). https://doi.org/10.1109/tpwrs.2021.3088259
31. Sioshansi, F.: Consumers, Prosumers, Prosumagers: How Service Innovations Will Disrupt the Utility. Tech. Rep. Elsevier, Amsterdam (2016)
32. Zhu, J., et al.: Bilateral inertia and damping emulation control scheme of vsc-hvdc transmission systems for asynchronous grid interconnections. IEEE Trans. Power Syst., 1–12 (2022)
33. Chen, Y., et al.: Accurate and general small-signal impedance model of lcc-hvdc in sequence frame. IEEE Trans. Power Deliv. 38(6), 1–13 (2023). https://doi.org/10.1109/tpwrd.2023.3307552
34. Zhu, J., et al.: Inertia emulation and fast frequency-droop control strategy of a point-to-point vsc-hvdc transmission system for asynchronous grid interconnection. IEEE Trans. Power Electron. 37(6), 6530–6543 (2022). https://doi.org/10.1109/tpel.2021.3139960

How to cite this article: Zhu, J., et al.: Supercapacitor-based coordinated synthetic inertia scheme for voltage source converter-based HVDC integrated offshore wind farm. IET Energy Syst. Integr. 6(1), 5–17 (2024). https://doi.org/10.1049/esi2.12137

APPENDIX A

System parameters

TABLE A1 Parameters of the offshore wind farm (OWF) system.

Parameter	Value
Rated OWF capacity S_n	1000 MVA
OWF nominal DC voltage u_{dcowf}	1.2 kV
OWF nominal AC voltage u_{ac}	0.69 kV
Transf. 1 ratio and connection method	35/0.69 Yd11
Transf. 2 ratio and connection method	230/35 Yd11
Rated wind speed	10 m/s
PMSG DC-link capacitor C_{dc}	0.028 F
Supercapacitor C_{sc}	6.7 F
Energy storage unit filter inductor L_{sc}	3.31×10^{-7} H
Energy storage unit resistance R_{sc}	1.18×10^{-5} Ω
Covered frequency range $[f_{min}, f_{max}]$	[49 Hz, 51 Hz]
Maximum synthetic inertia H_{max}	10 s
SC voltage range $[u_{scmin}, u_{scmax}]$	[400 V, 800 V]
Neutral SC voltage u_{sc0}	632.5 V

TABLE A2 Parameters of the VSC-HVDC system.

Parameter	Value
Rated VSC power S_{vsc}	1000 MVA
Nominal DC voltage u_{dc}	±400 kV
Nominal DC voltage u_{ac}'	230 kV
System frequency f_0	50 Hz
DC capacitor C	50×10^{-6} F
Shunt filter capacitive power Q_c	0.1 pu
Shunt filter quality factor r	50
Reactor inductance L	0.3 pu
Reactor inductance R	0.03 pu
DC cable resistance R_{dc}	$9 \times e^{-3}$ W/m
DC cable inductance L_{dc}	$3.3 \times e^{-4}$ H/m
AC cable resistance R_{ac}	$5.29 \times e^{-3}$ W/m
AC cable inductance L_{ac}	$1.4 \times e^{-5}$ H/m
Transformer ratio and connection method	230/330 Yd11

TABLE A3 Parameters of the synchronous system.

Parameter	Value
Rated generator power S_g	750 MVA
Terminal voltage V_g	20 kV
Inertia time constant H_{sg}	6.175 s
x_d, x_d', x_d''	1.8, 0.3, 0.25
x_q, x_q'', x_l	1.7, 0.55, 0.2
t_d', t_d'', t_q', t_q''	8, 0.03, 0.4, 0.5
Stator resistance R_s	0.0025
Turbine permanent droop R_p	0.05
Exciter regulator gain K_e	200
Exciter time constant T_a	0.001 s
Transformer ratio and connection method	330/20 Yd11

TABLE A4 Parameters of the controllers.

Type	Parameter	Value
DC/DC	Outer-loop controller (k_{p1}, k_{i1})	(3.5, 60)
	Inner-loop controller (k_{p2}, k_{i2})	(2,200)
MSC	Outer-loop controller (k_{p3}, k_{i3})	(1,50)
	Inner-loop controller (k_{p4}, k_{i4})	(1.2,20)
GSC	Outer-loop controller (k_{p5}, k_{i5})	(10,500)
	Inner-loop controller (k_{p6}, k_{i6})	(0.8,250)
	PLL (k_{p7}, k_{i7})	(60,1400)

(Continues)

TABLE A4 (Continued)

Type	Parameter	Value
WF-VSC	Outer-loop controller (k_{p8}, k_{i8})	(1,50)
	Inner-loop controller (k_{p9}, k_{i9})	(0.8,250)
	Voltage threshold u_{d1}	0.95 pu
	Voltage change rate threshold du_{d1}/dt	−5 pu/s
	Duration T_{hold}	200 ms
GS-VSC	Outer-loop controller (k_{p10}, k_{i10})	(15,100)
	Inner-loop controller (k_{p11}, k_{i11})	(0.8,250)
	PLL (k_{p12}, k_{i12})	(60,1400)
	u_{dc}/f droop gain	1.2

TABLE A5 Eigenvalues of the tested small signal model system.

λ	Eigenvalue	Damping ratio	f (Hz)
λ_3 & λ_4	−0.154 ± j0.243	0.535	0.039
λ_6 & λ_7	−1.44 ± j2.98	0.436	0.474
λ_{12} & λ_{13}	−5.91 ± j38.7	0.151	6.16
λ_{15} & λ_{16}	−11.9 ± j17.6	0.559	2.8

APPENDIX B

System state-space model

The topology of the OWF + VSC-HVDC system is shown in Figure 1, including the PMSG OWF, the VSC-HVDC system and the onshore grid. Permanent magnet synchronous generation OWF includes the supercapacitor and its controller, GSC and its controller, and AC network. The machine side and grid side of PMSG are decoupled due to the DC capacitor; so the machine-side control parameters have little effect on the whole system. This paper omits the small signal modelling of the generator, MSC and their controller and uses a constant power source to replace the WT active power PWT; while the modelling of VSC-HVDC system includes that of DC link, DC capacitor, converters and their controllers; the onshore grid modelling consists of a SG and loads.

State-Space Model of the PMSG OWF

1) Supercapacitor Energy Unit and Its Controller State Space Model

For the supercapacitor energy unit, its state variables $\Delta\mathbf{X} = [\Delta i_{sc}, \Delta u_{sc}]$, the input variables $\Delta\mathbf{U} = [\Delta v_t]$, the state matrix $\mathbf{A}_{sc}$ and the input matrix $\mathbf{B}_{sc}$ are

$$A_{sc} = \begin{bmatrix} -\frac{R_{sc}}{L_{sc}} & -\frac{1}{L_{sc}} \\ \frac{1}{C_{sc}} & 0 \end{bmatrix} B_{sc} = \begin{bmatrix} \frac{1}{L_{sc}} \\ 0 \end{bmatrix}$$

The small-signal equation for the DC/DC control system is as follows:

$$\begin{cases} \Delta\dot{z}_1 = k_{i1} \cdot \dfrac{u_{sc}^* - \Delta u_{sc}}{u_{sc0}} \quad \Delta\dot{z}_2 = k_{i2} \cdot \dfrac{i_{sc}^* - \Delta i_{sc}}{S_n/u_{sc0}} \\ \dfrac{u_{sc}^*}{u_{sc0}} = \sqrt{1 + \dfrac{4H_{sc}S_n}{C_{sc}f_0u_{sc}^2}\left(f_{owf} - f_0\right)} \\ \dfrac{i_{sc}^*}{S_n/u_{sc0}} = k_{p1} \cdot \dfrac{u_{sc}^* - \Delta u_{sc}}{u_{sc0}} + \Delta z_1 \\ \dfrac{\Delta v_t}{u_{sc0}} = k_{p2} \cdot \dfrac{i_{sc}^* - \Delta i_{sc}}{S_n/u_{sc0}} + \Delta z_2 \end{cases} \tag{A1}$$

where v_t is the DC/DC converter low-side voltage.

2) PMSG DC Capacitor State Space Model

$$\begin{cases} \Delta\dot{u}_{dc\_owf} = \dfrac{(\Delta P_{WT} - \Delta P_{SC} - \Delta P_{GSC})S_n}{C_{dc}u_{dc0}^2\Delta u_{dc\_owf}} \\ \Delta P_{GSC} = \Delta u_{d0}\Delta i_{d0} + \Delta u_{q0}\Delta i_{q0} \\ \Delta P_{SC} = \dfrac{\Delta v_t\Delta i_{sc}}{S_n} \end{cases} \tag{A2}$$

3) GSC and Its Controller State Space Model

The small-signal equation for the GSC outer loop is as follows:

$$\begin{cases} \Delta\dot{z}_3 = k_{i5}\left(\Delta u_{dc\_owf} - u_{dc\_owf}^*\right) \\ \Delta\dot{z}_4 = k_{i5}\left(\Delta Q_{owf} - \Delta Q_{owf}^*\right) \\ \Delta i_{d0}^* = k_{p5}\left(\Delta u_{dc\_owf} - u_{dc\_owf}^*\right) + \Delta z_3 \\ \Delta i_{q0}^* = k_{p5}\left(\Delta Q_{owf} - \Delta Q_{owf}^*\right) + \Delta z_4 \end{cases} \tag{A3}$$

The small-signal equation for the GSC inner current loop is as follows:

$$\begin{cases} \Delta\dot{z}_5 = k_{i6}\left(\Delta i_{d0}^* - \Delta i_{d0}\right) \\ \Delta\dot{z}_6 = k_{i6}\left(\Delta i_{q0}^* - \Delta i_{q0}\right) \\ \Delta u_{d0} = k_{p6}\left(\Delta i_{d0}^* - \Delta i_{d0}\right) + \Delta z_5 - \omega_{pll}L\Delta i_{q0} + \Delta u_{sd} \\ \Delta u_{q0} = k_{p6}\left(\Delta i_{q0}^* - \Delta i_{q0}\right) + \Delta z_6 + \omega_{pll}L\Delta i_{d0} + \Delta u_{sq} \end{cases} \tag{A4}$$

The small-signal equations for the PLLs are as follows:

$$\begin{cases} \Delta\dot{z}_{\omega} = k_{i7}\dfrac{\Delta u_{sq}}{\sqrt{\Delta u_{sd}^2 + \Delta u_{sq}^2}} \\ \Delta\dot{\theta} = \Delta\omega_{pll} \\ \Delta\omega_{pll} = k_{p7}\dfrac{\Delta u_{sq}}{\sqrt{\Delta u_{sd}^2 + \Delta u_{sq}^2}} + \Delta z_{\omega} \end{cases} \tag{A5}$$

4) OWF AC Network State Space Model

The OWF AC network consists of a transformer, line, and shunt filter. The OWF AC network input variables $\Delta\mathbf{U} = [\Delta u_{d0}\text{-}\Delta u_{d1},\ \Delta u_{q0}\text{-}\Delta u_{q1},\ \Delta i_{d0}\text{-}\Delta i_{d1},\ \Delta i_{q0}\text{-}\Delta i_{q1}]$, the state variables $\Delta\mathbf{X} = [\Delta i_{d0},\ \Delta i_{q0},\ \Delta u_{d1},\ \Delta u_{q1}]$, the state matrix $\mathbf{A}_w$ and the input matrix $\mathbf{B}_w$ are

$$\mathbf{A}_w = \begin{bmatrix} -\dfrac{R_{owf}}{L_{owf}} & \omega_{pll} & & \\ -\omega_{pll} & -\dfrac{R_{owf}}{L_{owf}} & \mathbf{O}_{2\times2} & \\ & & 0 & \omega_{pll} \\ \mathbf{O}_{2\times2} & & -\omega_{pll} & 0 \end{bmatrix}$$

$\mathbf{B}_w$

$$= \begin{bmatrix} \dfrac{1}{L_{owf}} & 0 & & \\ 0 & \dfrac{1}{L_{owf}} & \mathbf{O}_{2\times2} & \\ & & \omega_{pll}\dfrac{Q_c/r}{(Q_c/r)^2 + Q_c^2} & 0 \\ \mathbf{O}_{2\times2} & & 0 & \omega_{pll}\dfrac{Q_c/r}{(Q_c/r)^2 + Q_c^2} \end{bmatrix}$$

where Δu_{d1} and Δu_{q1} are the port voltages of the parallel filter in the dq-axis, respectively.

State-Space Model of the VSC-HVDC

The VSC-HVDC state space model is established in Ref. [34], including DC system, converters and their controllers.

State-Space Model of the Onshore Power Grid

The onshore power grid system is comprised of two main parts: SGs and the AC network. The detailed state space model is elaborated in Ref. [34].